

Solving the enigma: Deriving optimal explanations of deep networks

Michail Mamalakis^{1,2*}, Antonios Mamalakis^{3,4}, Ingrid Agartz⁷,
Lynn Egeland Mørch-Johnsen^{5,6}, Graham Murray¹,
John Suckling¹, Pietro Lio²

^{1*}Department of Psychiatry, University of Cambridge, Hills Road,
Cambridge, CB2 2QQ, Cambridgeshire, United Kingdom.

²Department of Computer Science and Technology, University of
Cambridge, 15 JJ Thomson Ave, Cambridge, CB3 0FD,
Cambridgeshire, United Kingdom.

³Department of Environmental Sciences, University of Virginia,
Charlottesville, Virginia, United States of America.

⁴School of Data Science, University of Virginia, Charlottesville,
Virginia, United States of America.

⁵Norment, Division of Mental Health and Addiction, Oslo University
Hospital, Institute of Clinical Medicine, University of Oslo, Oslo, Norway.

⁶Department of Psychiatry and Department of Clinical Research,,
Østfold Hospital, Grålum, Norway.

⁷Department of Psychiatric Research,, Diakonhjemmet Hospital, Oslo,
Norway.

*Corresponding author(s). E-mail(s): mm2703@cam.ac.uk;

Contributing authors: npa4tg@virginia.edu;

ingrid.agartz@medisin.uio.no; l.e.morch-johnsen@medisin.uio.no;

gm285@cam.ac.uk; js369@cam.ac.uk; pl219@cam.ac.uk;

Abstract

The accelerated progress of artificial intelligence (AI) has popularized deep learning models across domains, yet their inherent opacity poses challenges, notably in critical fields like healthcare, medicine and the geosciences. Explainable AI (XAI) has emerged to shed light on these "black box" models, helping decipher their

decision making process. Nevertheless, different XAI methods yield highly different explanations. This inter-method variability increases uncertainty and lowers trust in deep networks' predictions. In this study, for the first time, we propose a novel framework designed to enhance the explainability of deep networks, by maximizing both the accuracy and the comprehensibility of the explanations. Our framework integrates various explanations from established XAI methods and employs a non-linear "explanation optimizer" to construct a unique and optimal explanation. Through experiments on multi-class and binary classification tasks in 2D object and 3D neuroscience imaging, we validate the efficacy of our approach. Our explanation optimizer achieved superior faithfulness scores, averaging 155% and 63% higher than the best performing XAI method in the 3D and 2D applications, respectively. Additionally, our approach yielded lower complexity, increasing comprehensibility. Our results suggest that optimal explanations based on specific criteria are derivable and address the issue of inter-method variability in the current XAI literature.

Keywords: XAI, neuroscience, brain, 3D, 2D, computer vision, classification

Main

In the last decade, deep learning models have led to transformative changes across diverse domains, including the geosciences [1, 2], automotive engineering, healthcare [3–5], and biology [6, 7]. However, the inherent opacity of these sophisticated models, often likened to "black boxes," presents formidable challenges in comprehending their decision-making processes. In response to this challenge, the field of eXplainable Artificial Intelligence (XAI) has emerged as a pivotal area of research dedicated to explaining these black-box models and elucidating the rationale behind their predictions. Over the years, a multitude of XAI methods have been developed, all aimed at shedding light on how artificial intelligence (AI) arrives at specific predictions.

Explainable artificial intelligence can be broadly classified into two methodological approaches: inherently interpretable and post-hoc. Interpretable methods prioritize models endowed with properties such as simulatability, decomposability, and transparency, making them inherently comprehensible. Typically, these include linear techniques like Bayesian classifiers, support vector machines, decision trees, and K-nearest neighbor algorithms [8]. In contrast, post-hoc methods are employed alongside AI techniques in a post-prediction setting to explain the (otherwise non interpretable) AI predictions and unveil nonlinear mappings within complex datasets. In this manuscript, we will focus on post-hoc "local" methods that provide an explanation for each AI prediction separately, as opposed to post-hoc "global" methods that derive explanations for the decision-making of the AI for the entire dataset [9]. One notable post-hoc local technique is the local interpretable model-agnostic explanations (LIME), which explains the network's predictions by building simple interpretable models that approximate the deep network locally, i.e., in the close neighborhood of the prediction of interest [10]. Post-hoc techniques encompass model-specific approaches designed to address specific nonlinear model behaviors and model-agnostic approaches

to investigate data complexity [3, 8]. In computer vision, model-agnostic techniques such as LIME and perturbation-based methods find extensive application, while model-specific methods include feature relevance, condition-based explanation, and rule-based learning [8, 11, 12]. Similarly, in medical imaging, XAI methods predominantly consists of attribution and perturbation techniques [13]. Attribution techniques identify the important features for a given prediction by assigning relevance scores to features of a given input. Perturbation techniques assess the sensitivity of an AI prediction to certain input features [14], by systematically perturbing sub-groups of the input data [13, 15]. Among the XAI methods used in medical imaging, GRAD-CAM emerges as one of the most frequently employed techniques [15].

Despite the benefits and potential of XAI methods in advancing model trust, model fine-tuning and learning new science ([16]), recent studies have shown that they suffer from important pitfalls ([14, 17]). For instance, when using the $\alpha1\beta0$ rule of the method Layer-wise Relevance Propagation (LRP, an attribution method; [18]), explanations have been shown to be smooth and comprehensible but of lower accuracy/faithfulness to the deep network decision making ([14]). Reportedly, this is because the $\alpha1\beta0$ rule considers only the positive preactivations in the network ([14, 17]). Recent studies have suggested LRP modifications that combine various LRP rules to produce both faithful and smooth results ([19]). As a second example, SHapley Additive exPlnations (SHAP; [20]), an attribution method based on game theory principles, computes relevance scores called Shapley values for input features, for a given prediction. The primary challenge of implementing SHAP lies in accurately calculating the Shapley values by sampling all theoretically possible combinations of features (i.e., in line with game theory principles), due to constraints raised by computing resources. Several studies have utilized adapted Monte Carlo methods within the permutation space to achieve more precise sampling of Shapley values [21]. Moreover, efforts have been made to improve results by minimizing the weighted least square error of Shapley values estimation, leveraging learned parametric functions, as described in studies of Kernel-Shap and Fast-Shap [22]. Similarly, SVARM ([23]) employs stratified sampling by segmenting a dataset into sub-groups or strata and sub-sampling from each input instance. By combining mean estimates from all strata, this technique achieves a more precise estimation of the Shapley values and effectively mitigates the variance. Despite these efforts to optimize already established XAI methods, no existing XAI method has been proven to be consistently superior when considering various performance scores and properties that an ideal method should exhibit (e.g., faithfulness to the network decision making process, comprehensibility, robustness, localization; [24]). As such, a more holistic approach (implementing many methods) is typically preferred ([16]). However, even when explaining the same deep network and the same prediction, different XAI methods yield highly different explanations (see Fig. 1), increasing uncertainty about the decision making process of deep networks and lowering trust. The sub-optimal results of individual XAI methods combined with the high inter-method variability constitute one of the biggest challenges in the field of XAI currently.

In this study, for the first time, an "explanation optimizer" is proposed to derive an optimal explanation for deep classifiers in computer vision tasks, based on specific

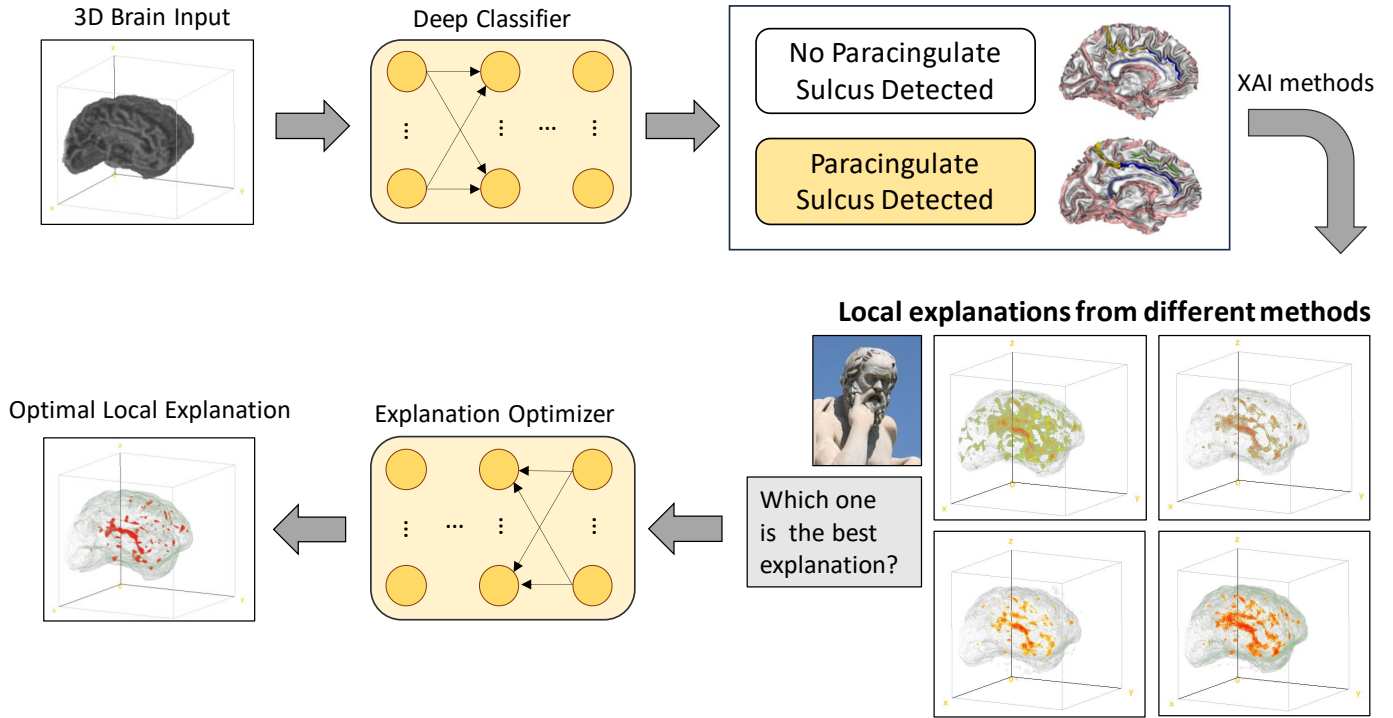
pre-defined performance metrics (see Fig. 1), thus, solving the enigma of explainability. The optimizer reconstructs a singular explanation by integrating the outputs of existing XAI methods. This approach ensures that the resulting explanation both accurately captures the essence of the network’s decision-making process (honoring faithfulness) and maximizes comprehensibility (minimizing complexity). The framework ultimately provides a unique optimal explanation with the same or higher resolution as the network’s input (see Fig. 2). We note that providing high resolution explanations is useful for more accurate identification of significant features, particularly crucial in medical applications [9]. To assess the effectiveness of our framework, we conducted experiments on both multi-class and binary classification tasks in two- and three-dimensional spaces, respectively, focusing on automobiles-animals and neuroscience imaging domains. For the three-dimensional task, we utilized a comprehensive dataset consisting of 596 subjects with 3D brain volumes, sourced from the TOP-OSLO study [25]. This dataset was employed for binary classification, specifically exploring the presence or absence of the paracingulate sulcus (PCS). The PCS is a variable secondary sulcus, which is associated with cognitive performance and hallucinations in patients with schizophrenia [26],[27]. For the two-dimensional multi-class task, we employed the CIFAR-10 dataset [28] a widely-used benchmark dataset, containing approximately 60,000 images across 10 different classes of animals and vehicles. In both experiments, we partitioned the datasets into training (60%), validation (20%), and testing (20%) subsets to ensure robust evaluation of our framework’s performance.

The explanation optimizers, employed in the 3D and 2D experiments, are presented in Fig. 2a. and b, respectively. In both cases, the optimizer is initiated with a layer of local explanations from various already-established XAI methods. A weighted average of these explanations is computed. The individual local explanations and the weighted average are then concatenated and fed into a deep learning network (non-linear structure) to reconstruct a unique, optimal explanation (see Methods section for more details). After the optimal explanation is derived, a high-resolution version is extracted by using an Up-Sampling layer (see Fig. 2a.b). Finally, for training, the cost function evaluates i) the similarity between the weighted average and low-resolution prediction, ii) the faithfulness score of the explanation as quantified in [24], and iii) the complexity score of the explanation as quantified in [24] (Fig. 2a.b). The similarity score above (i) is used in the loss function to constrain the optimization solution and to accelerate the training convergence. Additional details can be found in the Methods section.

The inspiration behind the proposed explanation optimizer is rooted in Herbert Simon’s seminal work on ”bounded rationality” and ”satisficing” decision-making [29, 30]. Bounded rationality acknowledges that individual rationality is constrained by the heuristics and biases humans employ to explain the world. Heuristics are cognitive rules individuals use in their daily lives to make routine decisions, while cognitive biases are specific beliefs or perspectives supported by evidence and reasoning. Thus, ”bounded rationality” recognizes the limitations of human knowledge, time, and computational power. Simon introduced the term “satisficing” in 1956, representing the concept where individuals seek solutions or accept choices that are ”good enough” for their purposes,

Fig. 1: Deriving optimal local explanations for deep classifiers in anatomical neuroscience.

Deriving Optimal Local Explanations for Deep Classifiers in Anatomical Neuroscience



The figure depicts the traditional local explanation process (implementing multiple XAI methods) for a three-dimensional binary classification example regarding the existence or absence of PCS (Paracingulate Sulcus Detected). This is one of the two case studies we consider in this paper. Note that the high variability in the local explanations that arises from different XAI methods increases uncertainty and lowers trust in explainability among experts. Therefore, an explanation optimizer is proposed to derive the optimal explanation for the pre-trained Deep Classifier in the computer vision task of interest.

even if they are not fully optimized [31]. This concept provides an alternative basis for decision-making modeling, complementing the traditional view of decision-making as optimization. Simon's ideas of bounded rationality and satisficing decision-making have gained widespread acceptance, influencing research across the social sciences. In our application, we leverage bounded rationality by integrating established knowledge from different XAI methods that may or may not be biased/bounded in different

ways. Additionally, our proposed cost function serves as a criterion for "satisficing" explanations in AI tasks.

To encapsulate, in this study, we propose a framework aimed at providing optimal explanations for pre-trained deep networks in specific computer vision tasks. Characterized by high faithfulness and low complexity, this framework ensures accuracy and comprehension in the provided explanations. Additionally, we develop a separate framework designed to deliver explanations in high-resolution spaces, enhancing our ability to capture and understand significant feature contributions effectively. Our framework is tested in applications across diverse domains, including automobiles, animals, and neuroscience, encompassing both 2D and 3D multi-classification and binary classification tasks. Finally, we formalize a generalized framework capable of optimizing explanations for N-dimensional inputs, extending the utility of our approach beyond specific computer vision tasks to offer a versatile solution for interpreting complex data across various dimensions and domains. Our results suggest that optimal explanations based on specific criteria are indeed derivable and address the issue of inter-method variability in the current XAI literature.

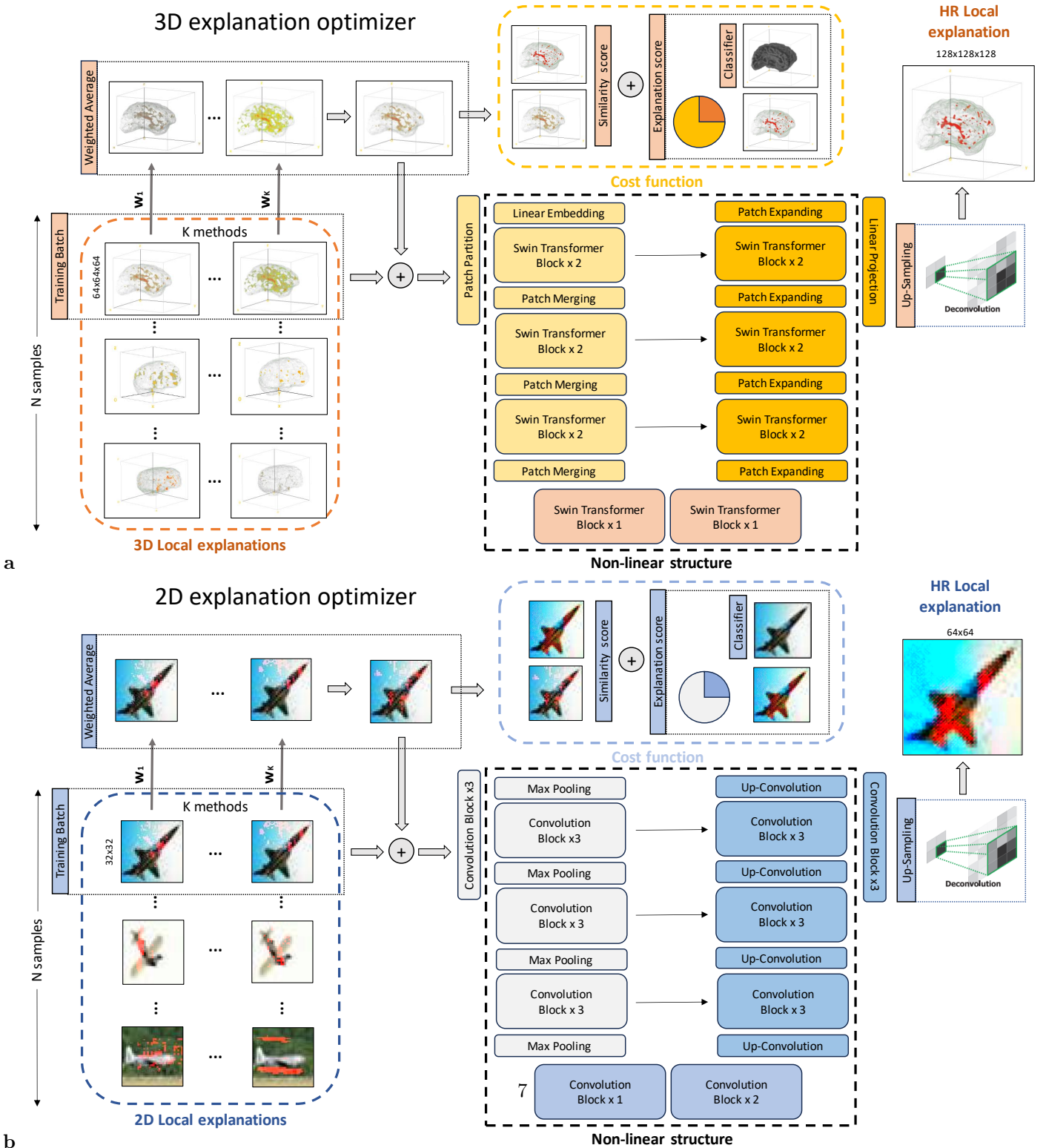
Results

Classification training and optimization of explanations

The deep neural networks were trained for binary and multi-label classification tasks, in two and three dimensional spaces. Hyperparameter tuning was conducted using a range of learning rates ($1e^{-2}$, $1e^{-3}$, $1e^{-4}$, $1e^{-5}$) to optimize performance for both tasks. The sensitivity of the results for these different learning rates is illustrated with light blue shading in Extended Data Fig. 1 a,b and c,d. Results show the minimum, median and maximum loss and accuracy values that the deep networks achieved in the training and validation datasets for the 3D and 2D applications, respectively. In the 3D binary classification task, the network achieved approximately 75.0% validation accuracy and around 70.0% training accuracy (Extended Data Fig. 1a,b). For the 2D multi-classification task, the highest validation accuracy exceeded 80.0%, with training accuracy surpassing 75.0%. Extended Data Fig. 1a-d. demonstrate the effective training of Resnet-18 and ResNet-50 models on Top-OSLO and CIFAR-10 datasets. The training and validation performance is shown to be fairly similar, indicating a low risk of overfitting. We note that the optimal learning rate for the three-dimensional application was found to be $1e^{-4}$, while for the two-dimensional application, it was $1e^{-2}$.

Next, Fig. 3a., and b. present the loss function during training of the explanation optimizer for each class in the 3D and 2D tasks. To train the explanation optimizer a separate hyperparameter tuning, utilizing different learning rates of $5e^{-2}$, $5e^{-3}$, $5e^{-4}$, and $5e^{-5}$, was performed. The light blue shading in Fig. 3a. and b. indicates the min and max loss values, while the solid curve represents the median loss across different learning rates. The best performance for the optimizer was achieved in the three-dimensional application for a learning rate of $5e^{-3}$ for the presence of PCS, $5e^{-4}$ for the absence of PCS, and $5e^{-3}$ for the two-dimensional scenario.

Fig. 2: The proposed framework in three and two dimension experiments.



The key components of the framework include the utilization of K baseline XAI methods (K methods), a 'Weighted Average' explanation, a non-linear network ('Non-linear structure'), and an 'Up-Sampling' unit. The framework incorporates a range of explanations obtained from established XAI methods and computes an adjusted baseline explanation ('Weighted Average'). The local explanations and the 'Weighted Average' are concatenated and fed into a suitably designed non-linear structure (Swin-UNETR (a) and U-Net (b)). The reconstructed optimal explanation feeds an upsampling deconvolution layer to increase the resolution (high-resolution (HR) local explanation). The cost function evaluates the similarity between the weighted average and the low-resolution prediction, which is added to the faithfulness and complexity scores of the explanation. **a)** The 3D application uses images from the Top-Oslo dataset ([25]). **b)** The 2D application uses images from the CIFAR-10 dataset ([28]).

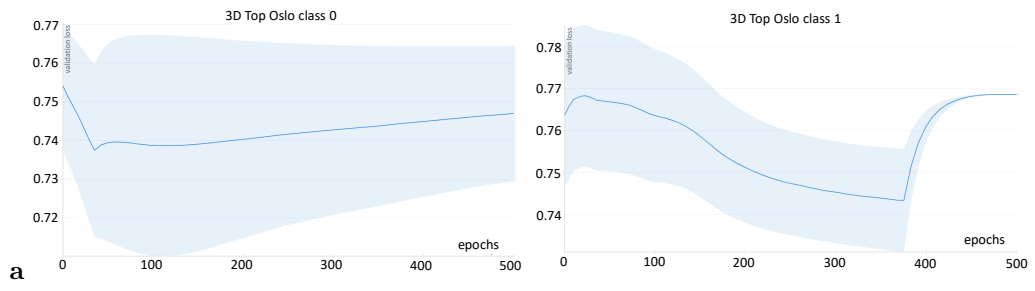
Explainability scores of the explanation optimizer

Fig. 4 presents the faithfulness and complexity scores obtained using various XAI methods alongside our proposed non-linear explanation optimizer for both the two and three-dimensional applications. In terms of faithfulness, our approach consistently outperforms other XAI methods, achieving higher average scores (exceeding 0.20 in 3D and 0.17 in 2D). Regarding complexity, our proposed approach demonstrates lower average values (below 12.15 in 3D and 9.35 in 2D), thus leading to more comprehensible explanations.

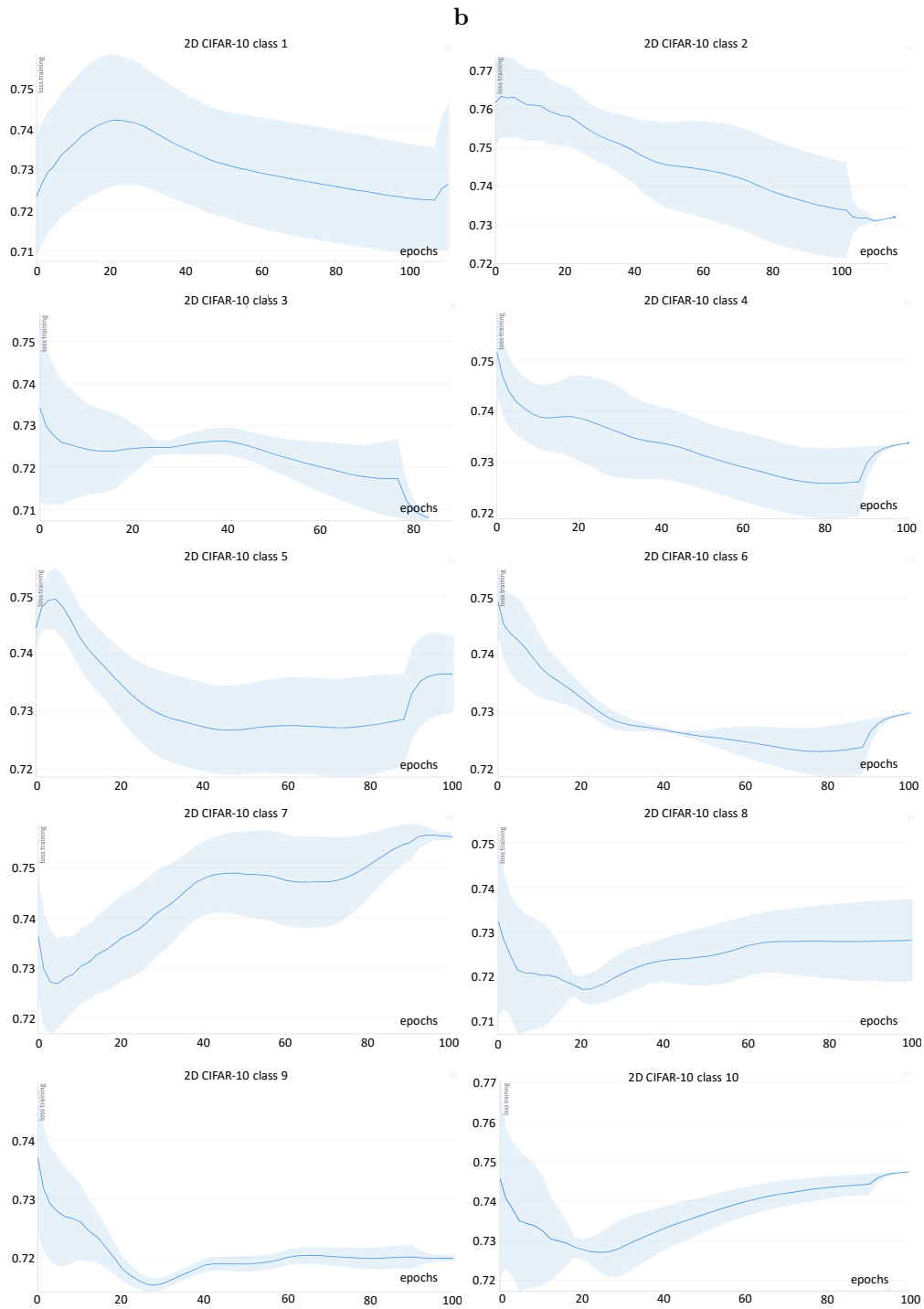
Statistical analysis, utilizing ANOVA two-sample tests, revealed highly significant differences between our proposed approach and the alternative XAI methods across all four cases of Fig. 4. Specifically, F values from our analysis were equal to 100.03, 168.02, 18.44, and 147.02 with corresponding F critical values equal to 1.8974, 1.9001, 1.8995, 1.8995 and for 3D faithfulness, 3D complexity, 2D faithfulness, and 2D complexity, respectively. Overall, these results verify that the proposed optimizer yields more optimal explanations than alternative XAI methods both in terms of faithfulness to the deep classifier and in terms of complexity, improving comprehensibility. Thus, our results provide new evidence that optimal explanations are indeed derivable and point to a new direction in XAI applications - that of combining existing methods to achieve higher level understanding of deep networks.

Fig. 5 a.,b.,c. present the explanations in the form of heatmaps, highlighting significant features for both the 3D and 2D applications. In the 3D application, Fig. 5 a., b. present two different examples where the Resnet-18 has successfully identified the absence and existence of PCS in the brain, respectively. The different panels show the important features of the 3D brain (sulci sub-regions in the medial view) that helped the network predict, as identified by different XAI methods and our explanation optimizer. In each case, all important features are presented in the first row, and the top 10% important features are shown in the second row. A significant variability is observed across the explanations provided by existing XAI methods like DeepLift, Kernel Shap, Gradient Shap etc., making it challenging to determine which the optimal explanation is. The explanation from our proposed optimizer ('Explanation Optimizer (non-Linear)') highlights the sub-regions of the areas where the PCS is usually expected to be located [32, 33] (Fig. 5 a. b). On the contrary, other XAI methods highlight areas that are not as typically related to the PCS connectomics (Gradient Shap; Fig. 5 a.,b. and DeepLift Shap; Fig. 5 b.).

Fig. 3: Explanation optimization of the 2D and 3D explanation training results

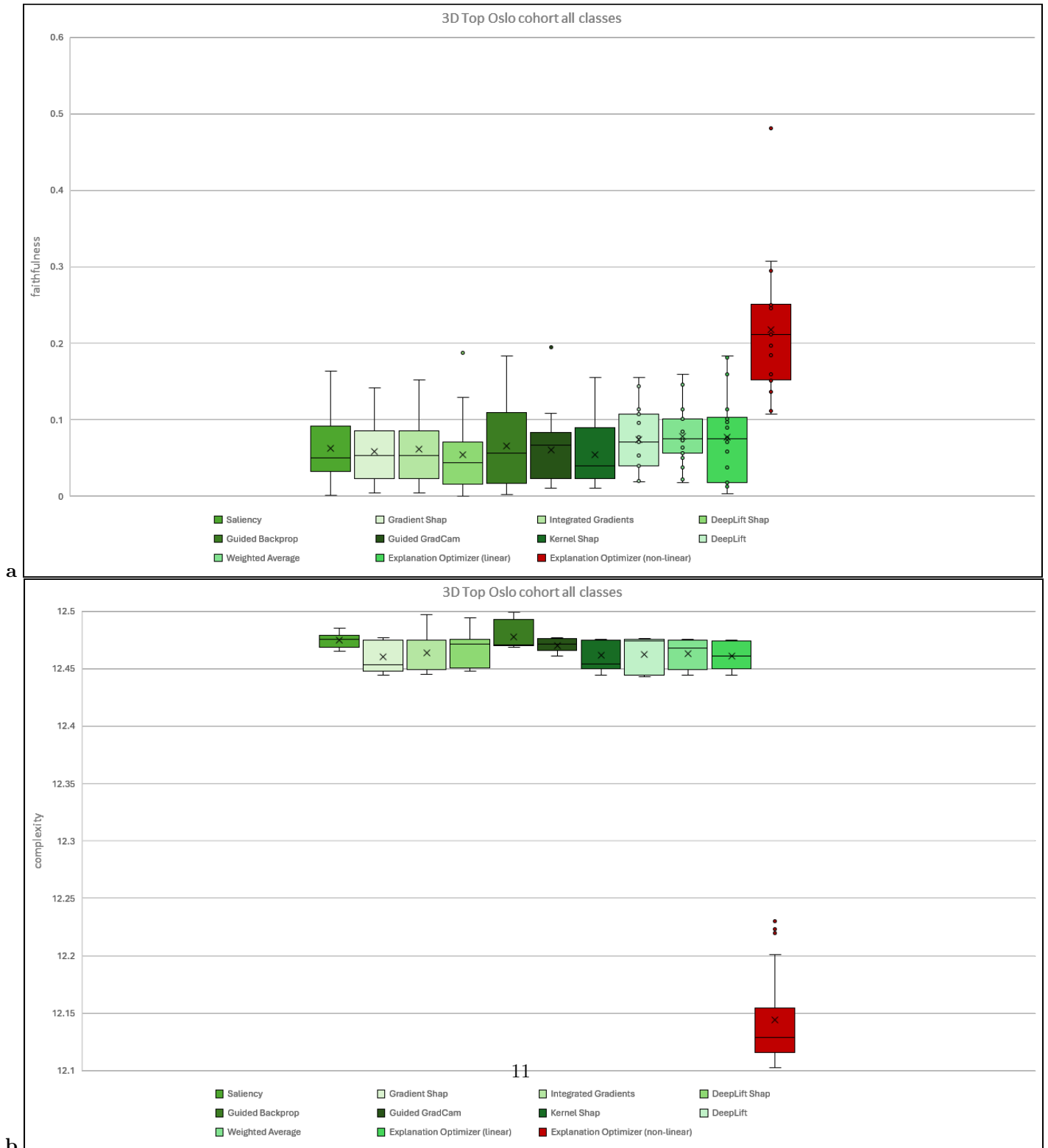


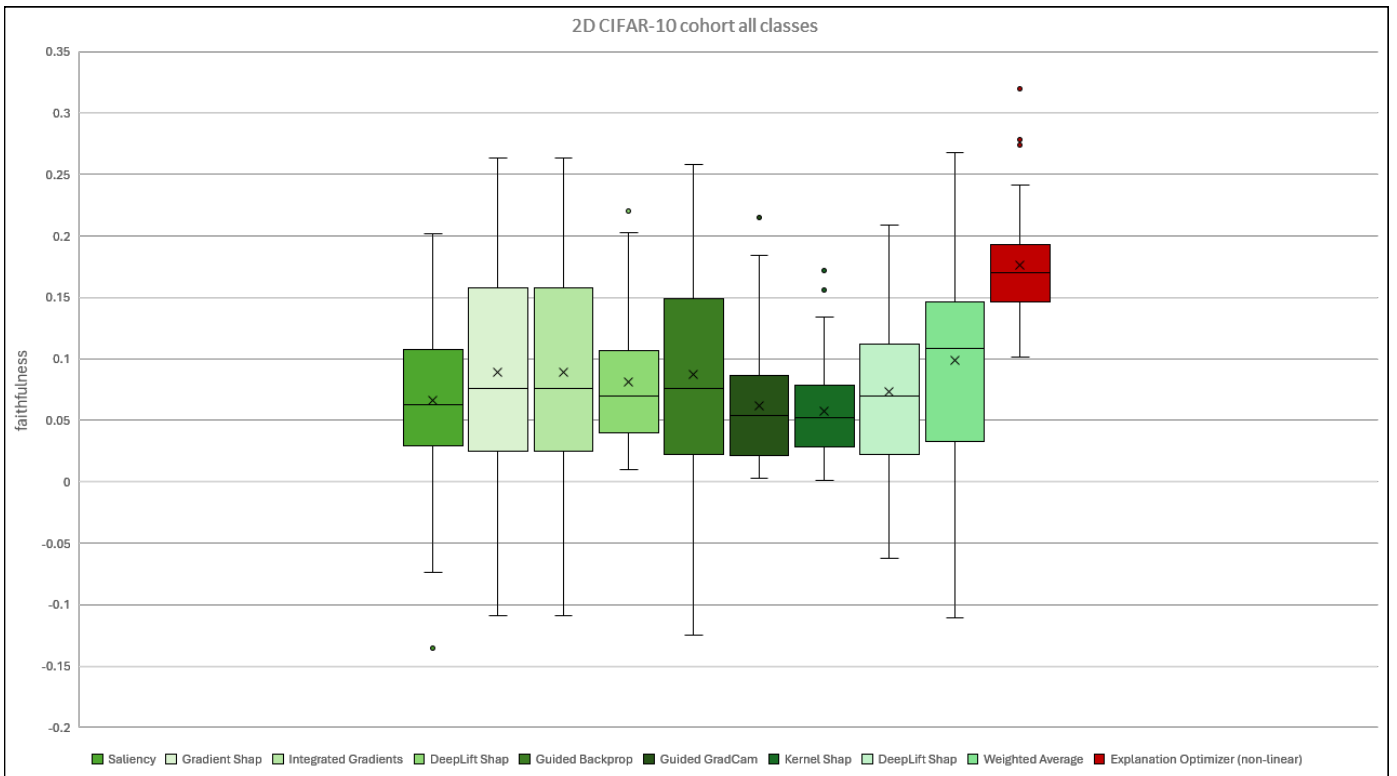
a



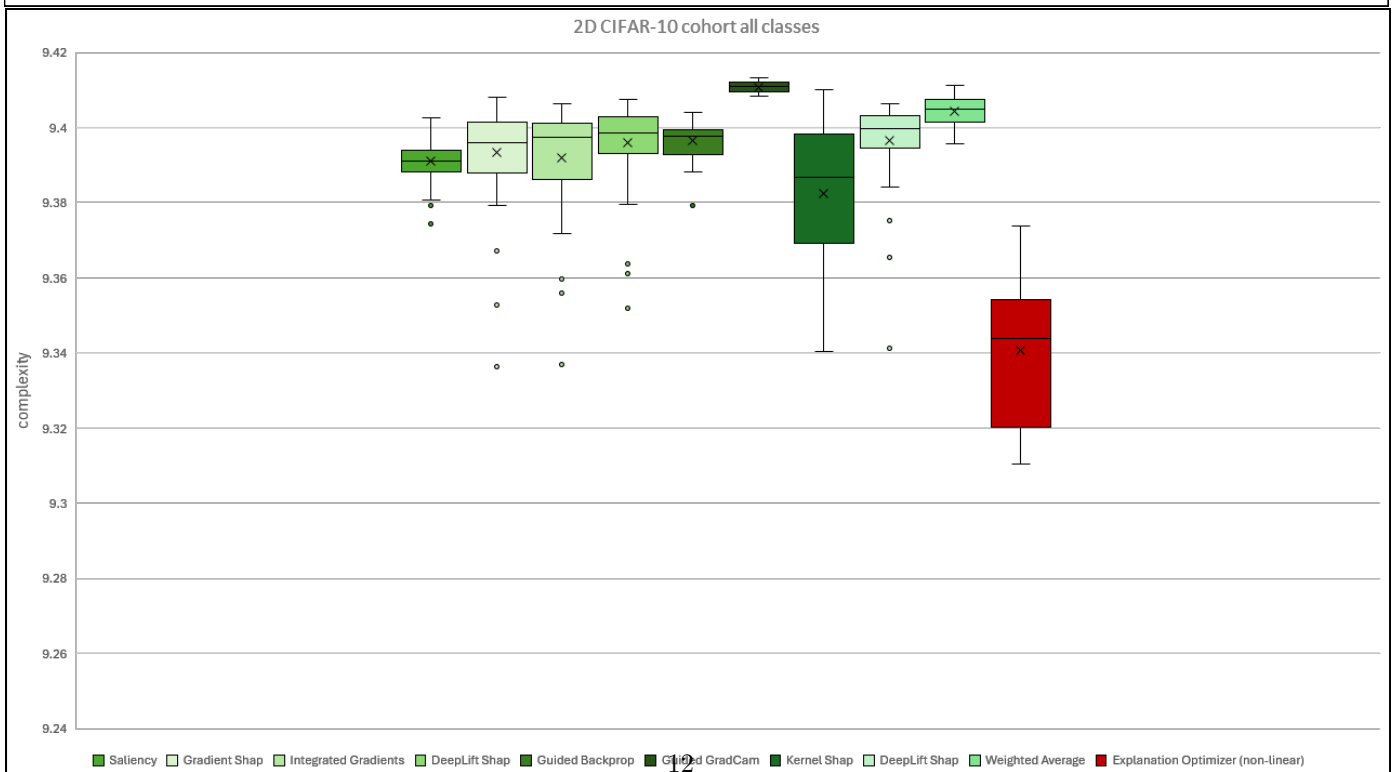
The light blue shading in the panels highlights the min/max and the median loss values obtained during training across various learning rates. **(a)** The sub-figures present the validation loss of the explanation optimizer for the binary classification task for class 0 (absence of PCS) and class 1 (existence of PCS) in the 3D brain application. **(b)** The sub-figures present the validation loss of the explanation optimizer for the multi-class classification task for the ten classes in the 2D automobile/animals application.

Fig. 4: Box plot results comparing state-of-the-art XAI methods with the proposed approach for both 3D and 2D applications in the testing cohorts.





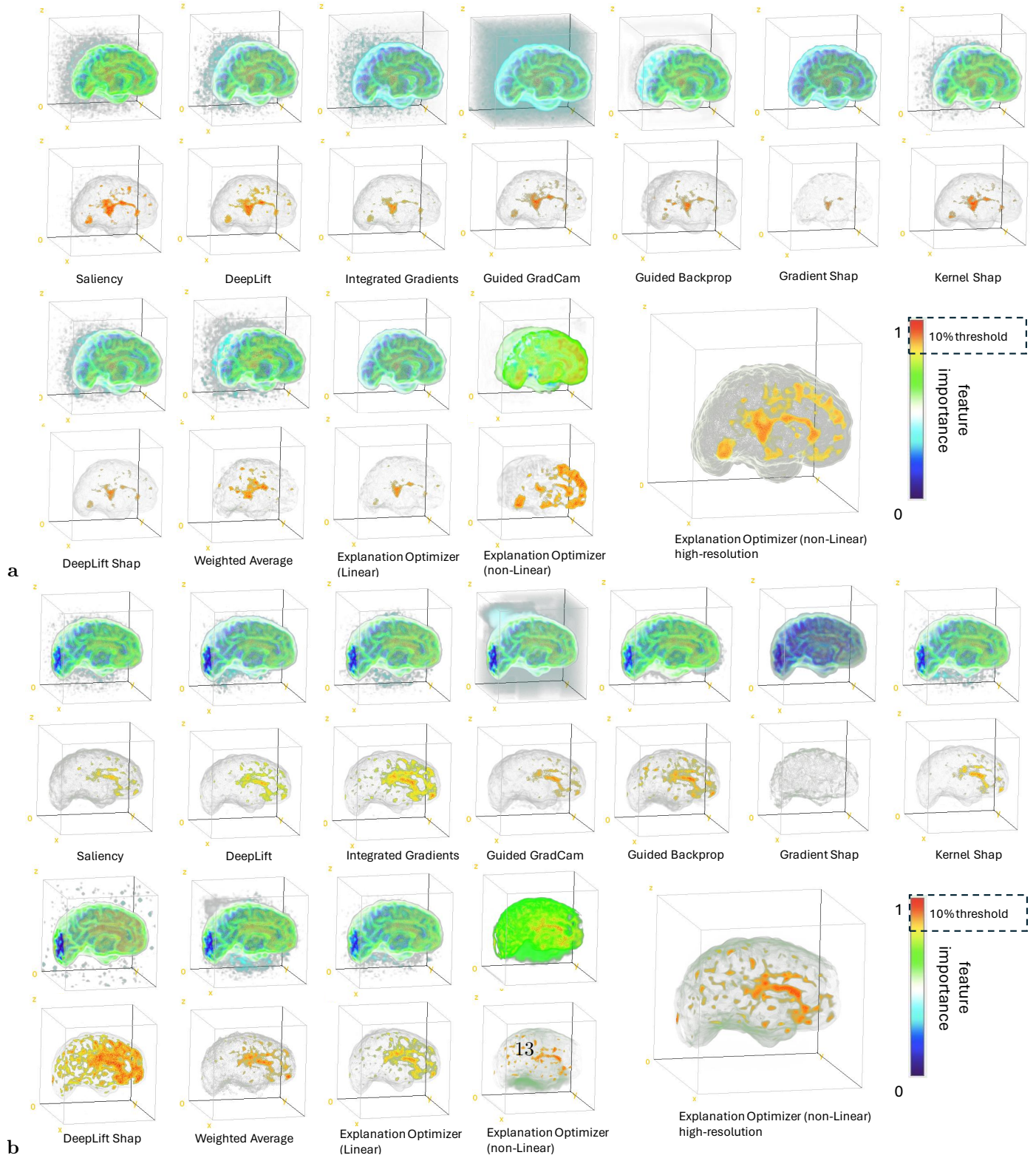
c

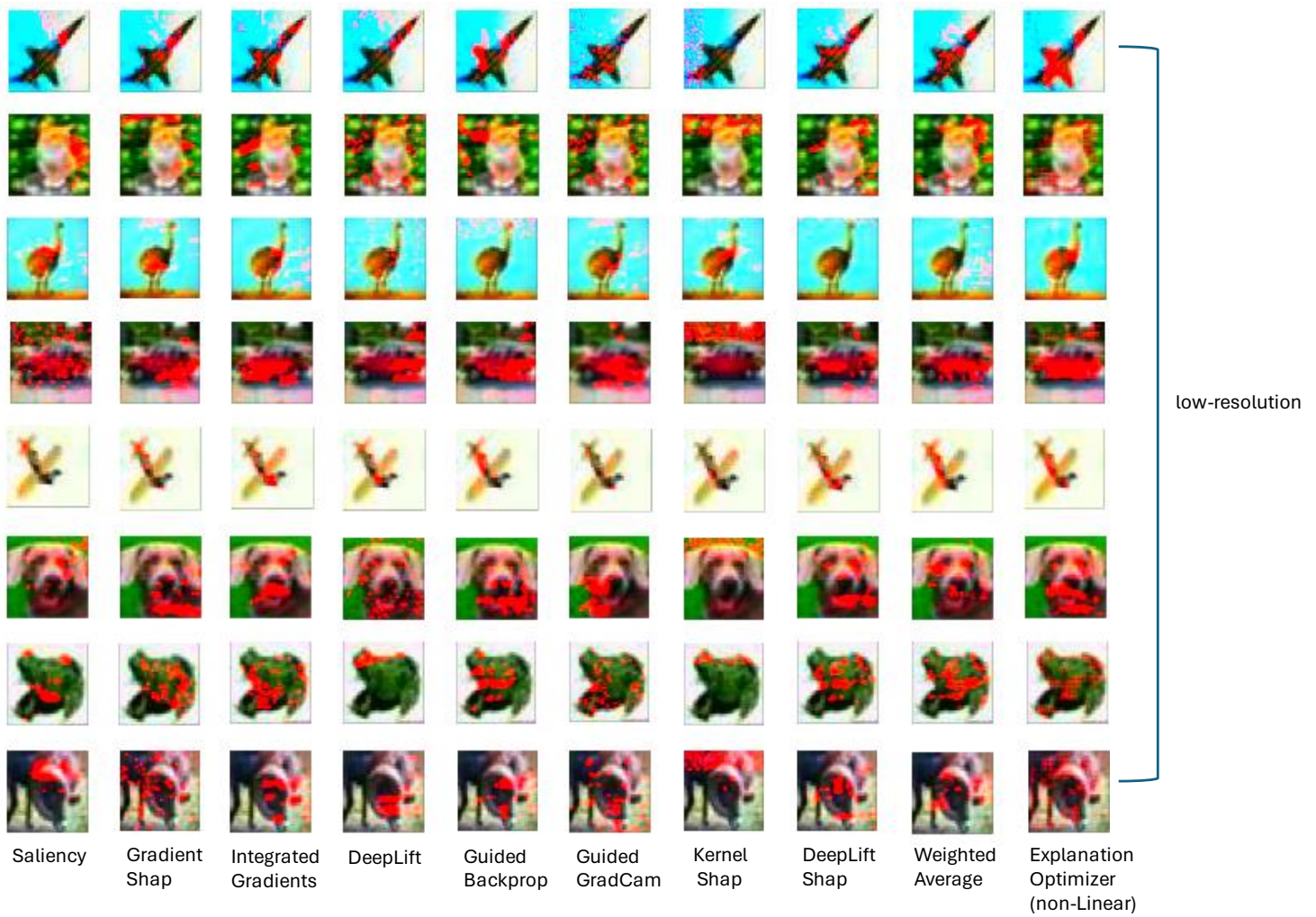


d

(a) The faithfulness score of different state-of-the-art XAI methods (green color variation) alongside the proposed linear and non-linear explanation optimizer (red color) for the 3D application. (b) Same as (a), but for the complexity score. (c-d) Same as (a-b), but for the 2D application.

Fig. 5: Visualization of the local explanations generated based on state-of-the-art XAI methods and the proposed explanation optimizer for both the 3D and the 2D applications.





c

● 10% threshold



Explanation Optimizer (non-Linear)
high-resolution

d

(a) The panels present the local explanations generated from different state-of-the-art XAI methods, alongside the results from the proposed explanation optimizer (the results of both linear and nonlinear implementations are presented), for the 3D application. Explanations are for a specific human individual, randomly selected from the test cohort of class 0 (absence of PCS). For each XAI method, the top row highlights the feature importance using a color scale from 0 to 1 (blue to red), while the second row highlights the most significant features based on a threshold of 10.0%. (b) Same as (a), but results are for a specific human individual, randomly selected from the test cohort of class 1 (existence of PCS). (c) Same as (a), but for the 2D application. Many different prediction instances are considered (different rows) and only the top 10.0% important features are shown. These explanations are for specific cases randomly selected from the test cohort of the classes: airplane, cat, bird, car, dog, frog, deer. These results are for low resolution (32×32). (d) Same as (c), but the high resolution explanations from our optimizer are presented (64×64).

Thus, the proposed explanation optimizer seems to deliver more realistic patterns than other XAI methods regarding which sub-regions contribute to the identification of the existence or absence of PCS ([32]). Also, the explanation from our optimizer exhibited the highest scores of faithfulness (see also Fig. 4.a), identifying regions of significance that align with results from the study [32]. Last, the proposed approach demonstrated less complexity (see also Fig. 4.b) and focused on specific sub-regions (Fig. 5 a., b.), advancing the understanding of the underlying mechanisms.

For the two-dimensional examples, explanations of many different prediction instances (airplanes, cats, birds, cars, dogs, frogs, and deers) are presented. For simplicity, only the top 10% important features are shown; see Fig. 5 c. The results suggest that our proposed method provides more accurate explanations of the network’s predictions compared to other XAI methods, emphasizing objects and foreground parts that are expected to be critical for classification. For instance, in the first airplane example (top row), saliency and DeepLift primarily focus on the airplane’s head, Kernel Shap focuses on the tail, and Gradient Shap focuses on the body and head, while our proposed optimizer identifies all parts of the air plane as significant features. Similar remarks are valid for the instances of the car classification, where the optimal explanation very explicitly identifies all the body parts of the car as important features to the network prediction.

Why utilizing a non-linear optimizer structure over linear alternatives?

A question that may arise is why we opted to use a non-linear structure in our proposed framework (see Fig. 2 and Fig. 6) to reconstruct the unique and optimal explanation for the deep learning network, instead of using a linear structure. To investigate this further, we explored a linearly structured optimizer (see Supplementary Fig. 1) and compared the results with the non-linear one. Specifically, in the 3D neuroscience application, where the complexity of the space is higher, we decided to further examine reconstruction structures beyond the non-linear approach, namely, encoder, bottleneck, and decoder with non-linear activations and blocks (non-linear structure, Fig. 6). Therefore, we employed a linear structure with attention mechanisms to estimate scalable weights to be used in a weighted average of the existing XAI methodologies (referred to in the subsection ‘Deep learning architecture’ of the Methods section). The baseline ‘weighted average’ mentioned in the Methods section and presented in Fig. 6 is considered as another linear approach employing fixed weights. Both linear approaches, whether employing fixed weights (‘Weighted Average’) or trainable weights (‘Explanation Optimizer (Linear)’), yielded comparable results to the existing XAI methods, as indicated in Fig. 4 a. and b. This suggests that linear solutions may not significantly outperform existing approaches in optimizing explanations for deep learning networks. Consequently, there is a rationale for exploring non-linear approaches, as done in this study. The results of a sensitivity analysis comparing the linear and non-linear structures for different learning rates are provided in the Supplementary material section, entitled ‘Sensitivity analysis for linear and non-linear structures’ (see Supplementary Fig. 2). The main observation is that the linear structure is more constrained in faithfulness and complexity scores during training,

ultimately converging to lower faithfulness and higher complexity scores compared to the non-linear structure. In contrast, the nonlinear structure exhibits a more stochastic behaviour during training, ultimately converging to a significantly more optimal solution.

Justifying the pursuit of optimal explanations for deep learning networks

In this study, we propose a method to address the challenge of identifying the optimal explanation among various XAI methods. We acknowledge in the manuscript that while adopting a holistic approach and using multiple XAI methods has been shown to be beneficial in some settings ([14, 16, 17]), it can result in highly different explanations, sometimes yielding overwhelming and incomprehensible outcomes, thus, lowering the trust to the network’s predictions. Our study demonstrates that opting to derive optimal explanations based on user-defined explainability quality metrics is feasible (see Fig. 4) and a promising alternative. Visual examples of explanations validate this claim, reinforcing the credibility of such an approach (see Fig. 5).

Deriving optimal explanations has been successfully achieved here by utilizing an innovative loss function. As a first component of the loss, we used the two scores of faithfulness and complexity, so as to ensure that the derived explanation is faithful to the network’s prediction-making process and maximally comprehensible. Additionally, we used a third term in the loss representing the similarity between the derived explanation and a baseline weighted average of explanations from existing XAI methods. By employing this similarity term, we further constrained the training of the optimizer, facilitated convergence and prevented divergence towards outlier and/or trivial solutions (e.g., red noise, impulse noise, etc.). By adjusting the importance of each one of these loss terms, one may formulate a unique cost function tailored to solve the problem of optimal explanation based on the needs of their application. We note that in our study, we chose the relative importance of these loss terms via hyper-parameter tuning (see Methods).

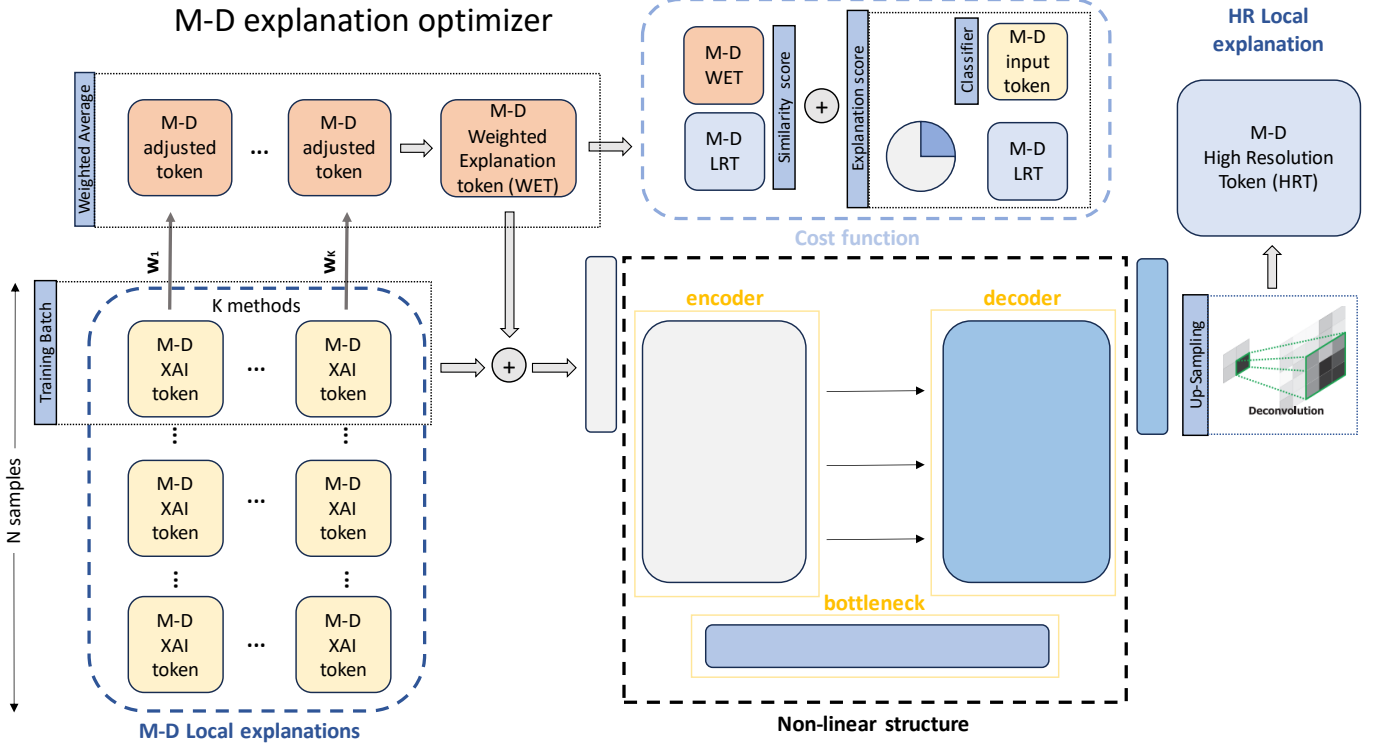
The final component of the proposed framework involved an Up-Sampling layer, aiming to provide a higher resolution explanation than the resolution of the prediction task (Fig. 6). This higher resolution explanation is vital, particularly in the domain of neuroscience, as it allows for the capture of more intricate details, enhancing the accuracy and comprehensiveness of the explanation. Fig. 5a. and b. show that the results from the ‘Explanation Optimizer (non-Linear) high-resolution’ are slightly different from compared to the results from the ‘Explanation Optimizer (non-Linear)’. The high resolution explanations are more in alignment with the given protocol for the identification of PCS ([32, 33]), supporting that the Up-sampling layer is a beneficial addition to our approach.

Beyond the two and three dimensions

We demonstrate our proposed framework in both 3D and 2D applications (Fig. 2a. and b.). For the sake of generalization of our proposed framework, we extended it to ‘ M ’ dimensions (i.e., referring to the input space), based on the principles outlined in

our approach (see Fig. 6). This generalized version can be adapted to any Artificial Intelligence application. Specifically, we denote ' K ' different XAI methods used as a baseline, with the '*input token*' representing the input features in a specific AI task of interest (see Fig. 6).

Fig. 6: The proposed framework for optimizing explanation extraction in M -dimensional space.



The generalized version of the proposed explanation optimizer in M dimensions. **M**: the number of dimensionality of the input space, **K**: the number of XAI methods used as baseline, **input token**: the input features for the AI task, **XAI token**: The local explanations from the baseline methods, $w_1..w_K$: The assigned weights based on the scoring of each XAI method on different explainability metrics (here complexity and faithfulness), **adjusted token**: The weighted product of w_1, w_2, \dots, w_K and the XAI token, **Weight Explanation Token (WET)**: the weighted average based on the K adjusted tokens of XAI methods, the **High Resolution Token (HRT)** represents the high resolution version of the optimal explanation after the 'non-linear structure' layer. **Low Resolution Token (LRT)** represents the low resolution that is the resolution of the input token.

The '*XAI token*' represents the essential features needed for the local explanation, generated by the baseline XAI methods. Furthermore, we denote different assigned

weights $w_1 \dots w_k$ derived from explainability metrics such as complexity and faithfulness, and we use the term '*adjusted token*' to refer to the products of the weights $w_1, w_2, \dots w_k$ with the XAI tokens. We define the '*Weighted Explanation Token (WET)*' as the weighted-average product derived from the adjusted tokens of the XAI methods. Additionally, the '*High Resolution Token (HRT)*' represents the high-resolution space post the 'non-linear structure' layer in the explanation optimization process, while the '*Low Resolution Token (LRT)*' denotes the input token's low-resolution space.

The proposed generalized framework illustrated in Fig. 6 can be applied to enhance explanations across domains such as large language models, multi-modality frameworks, video preprocessing, computer vision models, vision large models, foundation models, etc. with minor modifications to the non-linear structure of the encoder-decoder architecture to suit the specific task at hand.

Discussion

The importance of explainability, particularly in critical sectors like healthcare, medicine and the geosciences cannot be overstated. The opacity of deep learning models poses challenges in comprehending their decision-making processes, driving the need for robust methodologies for explainability. However, the high inter-method variability observed in explanations generated by existing XAI methods increase uncertainty and raises questions regarding the true explanation of deep learning networks in computer vision tasks. On top of this, it has been shown that no existing method is optimal across different quality metrics and for various prediction tasks and settings. Hence, there is a necessity for exploring ways to derive unique and optimal explanations building upon existing post-hoc XAI methods and guided by user-defined evaluation metrics. The uniqueness of the derived explanation directly address the issue of the current inter-method variability, while at the same time ensuring explanation optimality.

Our study explores the degree to which such an explanation is even derivable. Our proposed framework, inspired by Herbert Simon's seminal work on "bounded rationality" and "satisficing" decision-making, is shown to be able to derive such a unique and optimal explanation for pre-trained deep learning networks, tailored to specific computer vision tasks. By integrating diverse explanations from established XAI methods, employing a non-linear network architecture and an innovative loss function, we achieve to reconstruct a unique explanation that faithfully captures the essence of the network's decision-making process and minimizes complexity. To validate our framework, we conducted experiments on multi-class and binary classification tasks in both two- and three-dimensional spaces, focusing on automobiles-animals and neuroscience imaging domains.

Our results demonstrate the effectiveness of the framework in achieving high faithfulness and low complexity in explanations. Statistical analysis revealed significant differences between our approach and alternative state-of-the-art methods, further affirming its efficacy. Visual explanations provided by our framework offer insights into the decision-making process of deep learning models. In two-dimensional scenarios, our approach consistently outperformed other XAI methods, emphasizing significant

features crucial for classification. In three-dimensional applications, our framework showcased less complexity and focused on specific areas, advancing our understanding of underlying mechanisms. Our study also discusses the rationale behind favoring non-linear optimizing structures over linear alternatives. While linear solutions demonstrate comparable performance to the state-of-the-art XAI methods, non-linear approaches offer greater flexibility and accuracy in optimizing a highly faithful and less complex explanation for deep learning networks. Our optimizer is successful in part because of the utilization of a unique cost function that consists of explainability scores and a similarity score that constraints the convergence of the optimizer and avoids reaching non meaningful, trivial solutions during training. The generalized version of the proposed framework can be used in any explanation task of a N-dimensional space.

In terms of future research, the current framework could be expanded to include more explainability metrics in the loss function, beyond faithfulness and complexity that were used here as a first step, for example, robustness, localization etc. Moreover, one could explore whether similar explanation-optimizing frameworks can be derived for global explanation settings. Last, future work should focus on expanding the current framework in including layers that allow the quantification of uncertainty of the explanations. Such an addition shall further assist in drawing robust conclusions about the decision-making process of deep networks.

In conclusion, our framework represents a significant advancement in the field of XAI, offering a systematic and generic approach to optimizing the explainability of deep learning models. By providing optimally faithful and comprehensible explanations, our framework enhances trust and interpretability, paving the way for broader adoption of AI technologies in critical domains such as healthcare and medicine.

Methods

Evaluation metrics for the explanation

A crucial aspect of this study lies in evaluating "how accurate and comprehensive is an explanation?" To derive a useful explanation, two primary scores play a pivotal role: fidelity and complexity. An intuitive way to assess the quality of an explanation is by measuring its ability to accurately capture how the predictive model reacts to random perturbations [34]. For a deep neural network f , and input features \mathbf{x} , the feature importance scores (also known as "attribution scores") are derived in a way such that when we set particular input features \mathbf{x}_s to a baseline value \mathbf{x}_s^f , the change in the network's output should be proportional to the sum of attribution scores of the perturbed features \mathbf{x}_s . We quantify this by using the Pearson correlation between the sum of the attributions of \mathbf{x}_s and the difference in the output when setting those features to a reference baseline [35]. Thus, we define the faithfulness of an explanation method g as:

$$M_{faith}(f, g; \mathbf{x}) = corr_S(\sum_{i \in S} g(f, \mathbf{x})_i, f(\mathbf{x}) - f(\mathbf{x}[\mathbf{x}_s = \mathbf{x}_s^f])) \quad (1)$$

where S is a subset of indices ($S \subseteq [1, 2, 3 \dots d]$), \mathbf{x}_s is a sub-vector of an input \mathbf{x} ($\mathbf{x} = \mathbf{x}_s \cup \mathbf{x}_f$ and \mathbf{x}_f the unchanged features of \mathbf{x} image). The total number of the \mathbf{x}_s sub-vectors, which partition an image is d . We denote as \mathbf{x}_s the changed features, and \mathbf{x}_f the unchanged features of \mathbf{x} image.

If for an image \mathbf{x} , explanation g highlights all d features, then it may be less comprehensible and more complex than needed (especially for large d). It is important to compute the level of complexity, as an efficient explanation has to be maximally comprehensible [35]. If P_g is a valid probability distribution and the $P_g(i)$ is the fractional contribution of feature x_i to the total magnitude of the attribution, then we define the complexity of the explanation g for the network f as:

$$M_{complex}(f, g; \mathbf{x}) = \sum_{i=1}^d P_g(i) (\log(\frac{1}{P_g(i)})) \quad (2)$$

where:

$$P_g(i) = \frac{|g(f, \mathbf{x})_i|}{\sum_{j=1}^d |g(f, \mathbf{x})_j|} \quad (3)$$

In order to evaluate these two explainability metrics, we used the software developed by [24]. This software package is a comprehensive toolkit that collects, organizes, and evaluates a wide range of performance metrics, proposed for explanation methods. We note that we used a zero baseline ('black'; $\mathbf{x}_s^f = \mathbf{0}$), and 70 random perturbations to calculate the Faithfulness score.

Overview of the proposed framework

The proposed framework entails an optimization approach aimed at attaining the highest faithfulness and lowest complexity of an explanation tailored to a specific deep learning network and computer vision task. Key components of the framework include the utilization of K baseline XAI methods, a 'Weighted Average' explanation, a non-linear network ('Non-linear structure'), and an Up-Sampling unit (Fig. 2). The framework incorporates a range of explanations obtained from established XAI methods and computes a adjusted baseline explanation by averaging these explanations based on assigned weights ('Weighted Average'). The assigned weights are computed from the equation below:

$$w_k = l_1 M_{faith}^k(f, g; \mathbf{x}) + l_2 M_{complex}^k(f, g; \mathbf{x}) \quad (4)$$

where l_1 and l_2 represent fixed values ranging from 0 to 1, signifying the contributions of faithfulness and complexity, respectively, to the final weighted average. In this study, we analyzed predictions and explanations for ten randomly selected prediction instances from the validation cohort. We assessed the faithfulness and complexity scores for each of the K explanation methods and for each prediction instance. Subsequently, we calculated the average faithfulness and complexity scores across the ten prediction instances and determined the final assigned weights using eq. 4 with $l_1 = 0.6, l_2 = 0.4$. The average values of $M_{faith}^K(f, g; \mathbf{x})$, $M_{complex}^K(f, g; \mathbf{x})$ and the assign weights w_k were normalized to range from 0 to 1.

The K explanations generated by the baseline XAI methods are fed into a non-linear network consisting of an encoder, bottleneck, and decoder architecture (see later sections for more details), with the objective of reconstructing a unique explanation. Following this, the reconstructed explanation undergoes sequential processing through an up-sampling deconvolution layer to double resolution. In our case, the resolutions of the 3D inputs in the application were $64 \times 64 \times 64$, while for the 2D images, they were 32×32 . The final output of our explanation of optimizing framework consists an up-sampled higher-resolution explanation based on the input ($128 \times 128 \times 128$ and 64×64) and an explanation with the same resolution as the input ($64 \times 64 \times 64$, and 32×32). The up-sampling approach is motivated by the aim to enhance the detail of the explanation. We note that particularly in neuroscience and medical applications, a higher resolution is closely linked with increased trust of the community to AI procedures, making the provision of explanations in both higher and intial resolutions highly desirable.

The down-sampled version of the explanation is evaluated using the faithfulness eq. 5 and complexity score eq. 2. Both the up-sampled and down-sampled explanations are evaluated as to their similarity to the 'Weighted Average' explanation. These three components (faithfulness, complexity, similarity) together constitute the cost function of the proposed optimization methodology.

The similarity score between the derived explanation and the 'Weighted Average' explanation is as follows:

$$SSIM(\mathbf{x}, \mathbf{y}) = 1 - \frac{(2\mu_x\mu_y + c_1)(2\sigma_{xy} + c_2)}{(\mu_x^2 + \mu_y^2 + c_1)(\sigma_x^2 + \sigma_y^2 + c_2)} \quad (5)$$

$$loss_{sim}(\mathbf{x}, \mathbf{y}) = \lambda_1 SSIM(\mathbf{x}, \mathbf{y})^{LR} + \lambda_2 SSIM(\mathbf{x}, \mathbf{y})^{HR} \quad (6)$$

where \mathbf{x} represents the derived explanation by our optimizer, \mathbf{y} denotes the 'Weighted Average' explanation, μ_x indicates the average of \mathbf{x} , σ_x signifies the variance of \mathbf{x} , σ_{xy} represents the covariance of \mathbf{x} and \mathbf{y} , and c_1 and c_2 are two variables utilized to stabilize the division with a weak denominator [36]. $SSIM(\mathbf{x}, \mathbf{y})^{LR}$ refers to the similarity score between the 'Weighted Average' explanation and the down-sampled predicted explanation (low resolution), while $SSIM(\mathbf{x}, \mathbf{y})^{HR}$ signifies the similarity score between a tri-linear or bicubic (in 3D and 2D space respectively) up-sampled 'Weighted Average' explanation and the derived high-resolution explanation. The values of λ_1 and λ_2 were fixed at 0.5 each. The total loss function was given by:

$$loss_{total}(\mathbf{x}, \mathbf{y}) = l_1 M_{faith}(f, g; \mathbf{x}) + l_2 M_{comp}(f, g; \mathbf{x}) + l_3 loss_{sim}(\mathbf{x}, \mathbf{y}) \quad (7)$$

Following an ablation study exploring various combinations of l 's in the above cost function, we determine that setting $l_1 = 0.5, l_2 = 0.3$, and $l_3 = 0.2$ is optimal. This selection ensures a balanced optimization approach that effectively addresses the unique challenge of deriving an optimal explanation.

The experiments in 3D and 2D applications

We assess the proposed framework in two distinct spatial domains: three-dimensional (3D) and two-dimensional (2D). Our objective is to evaluate the applicability of the proposed framework across various dimensionalities of computer vision inputs.

In the 3D application, our focus is on a binary classification task concerning the presence or absence of the paracingulate sulcus (PCS). Leveraging a comprehensive cohort of 596 subjects from the TOP-OSLO study [25], we divide the dataset into training (60%), validation (20%), and testing (20%) sets. For the 3D classification task, we utilize white-grey surface matter images extracted from T1-weighted MRI scans of patient brains. Our image preprocessing follows the outlined steps in [5]. For the 2D application, we utilize the publicly available CIFAR-10 dataset (<https://paperswithcode.com/dataset/cifar-10>). This dataset, a subset of the Tiny Images dataset, consists of 60,000 color images with dimensions of 32×32 . Each image is associated with one of 10 mutually exclusive classes, such as airplane, automobile, bird, cat, deer, dog, frog, horse, ship, and truck. The dataset is organized into training (60%), validation (20%), and testing (20%) sets, with 6,000 images per class.

Deep learning architectures

In this study, we utilized a Resnet-18 and a ResNet-50 network architectures [37] for the classification tasks in three-dimensional (3D) and two-dimensional (2D) settings, respectively.

With regards to the explanation optimizer, for the 3D application, we employed the Swin-UNETR architecture [38] as our non-linear reconstruction network, featuring a 24-feature size (Fig. 2 a.). For the 2D explanation optimization, we utilized a U-NET encoder-decoder architecture [39] (Fig. 2 b.).

As part of an ablation analysis (see Results), we explored a linear implementation in the three-dimensional application. Here, we employed visual transformer encoders [40] to estimate weights for each of the K explainable baseline methods (refer in Supplementary material subsection: 'Deep learning architectures: The linear implementation of the proposed network'). Subsequently, these estimated weights were utilized in a weighted average to extract the linearly optimized explanation.

The baseline XAI methods

For this study, we employed eight established XAI methods: Saliency[20], DeepLift[20], Kernel Shap[20], DeepLift Shap[20], Integrated Gradients [41], Guided Backpropagation [42], Guided GradCam [43] and Gradient Shap. GradientShap makes an assumption that the input features are independent and that the explanation model is linear, meaning that the explanations are modeled through the additive composition of feature effects. Under these assumptions, SHAP values [20] can be approximated as the expectation of gradients computed for randomly generated n samples from the input dataset. Gaussian noise is added n times to each input, creating different baselines for computing the SHAP values.

Extending the implementation of these explainability approaches from two-dimensional (2D) to three-dimensional (3D) space was necessary. We utilized the

Python software developed by [24] as the underlying libraries for our implementation. Further implementation details can be found in the public GitHub repository associated with this study. It’s important to note that all explanations were modified to focus exclusively on positive attributions. Any negative attribution in the original explanations were replaced with a zero value.

The hyperparameter utilization

For both the 2D and 3D classification tasks, after randomly shuffling the data, each dataset underwent splitting into training, validation, and testing sets, with proportions of 60%, 20%, and 20% of the total number of images, respectively. Sparse categorical cross-entropy was employed as the cost function, while the Adam algorithm [44] was utilized to optimize the loss function. Initially, the learning rate remained fixed for the first 300 epochs, followed by a decrease of 0.1 every 100 epochs. To prevent overfitting, an early stopping criterion of 100 consecutive epochs was enforced, with a maximum of 500 epochs used for the input modalities in the corresponding 2D and 3D applications. Data augmentation techniques were applied, including rotation (around the center of the image by a random angle from the range of $[-15^\circ, 15^\circ]$), width shift (up to 20 pixels), height shift (up to 20 pixels), and Zero phase Component Analysis (ZCA; [45]) whitening (adding noise to each image). Hyperparameter tuning was conducted for both applications using four different values of initial learning rates: $1e^{-2}$, $1e^{-3}$, $1e^{-4}$, and $1e^{-5}$ for the 2D application, and $5e^{-2}$, $5e^{-3}$, $5e^{-4}$, and $5e^{-5}$ for the 3D application.

The same fixed step learning rate and optimization algorithm, namely the Adam algorithm [44], were employed to optimize the loss function in the explainability task. However, no data augmentation techniques were utilized to train the optimizer. The cost function used was that of eq. 7. For the 2D task, the maximum number of epochs was set at 150, with an early stopping criterion of 10 epochs applied after passing the first 90 epochs. For the 3D task, the maximum number of epochs was set at 500, with an early stopping criterion of 120 epochs applied after the initial 300 epochs. Once again hyperparameter tuning was conducted for both applications using four different values of initial learning rates: $1e^{-2}$, $1e^{-3}$, $1e^{-4}$, and $1e^{-5}$ for the 2D application, and $5e^{-2}$, $5e^{-3}$, $5e^{-4}$, and $5e^{-5}$ for the 3D application.

Code and dataset availability

This study used the datasets of the TOP-OSLO [25] which can be obtained from University of Oslo upon request, subject to a data transfer agreement. The code developed in this study is written in the Python programming language using Keras/TensorFlow (Python) libraries. For the training and testing of deep learning networks, we have used an NVIDIA cluster with 4 GPUs and 64 GB RAM memory. We used an NVIDIA A100-SXM-80GB GPU, and the code will be publicly accessible through github.

Supplementary information. The manuscript contains supplementary material.

*

Acknowledgment All research at the Department of Psychiatry in the University of Cambridge is supported by the NIHR Cambridge Biomedical Research Centre (NIHR203312) and the NIHR Applied Research Collaboration East of England. The views expressed are those of the author(s) and not necessarily those of the NIHR or the Department of Health and Social Care. We acknowledge the use of the facilities of the Research Computing Services (RCS) of University of Cambridge, UK. GKM consults for ideo digital health. All other authors declare that they have no competing interests.

*

Author information

*

Authors and Affiliations

Department of Psychiatry, University of Cambridge, Cambridge, UK.

Michail Mamalakis, Graham Murray, John Suckling

Department of Environmental Science, University of Virginia, Charlottesville, Virginia, United States.

Antonios Mamalakis

Department of Computer Science and Technology, Computer Laboratory, University of Cambridge, Cambridge, UK.

Michail Mamalakis, Pietro Lio

Department of Psychiatric Research, Diakonhjemmet Hospital, Oslo, Norway

Ingrid Agartz

Norment, Division of Mental Health and Addiction, Oslo University Hospital, Institute of Clinical Medicine, University of Oslo, Oslo, Norway.

Lynn Egeland Mørch-Johnsen **Department of Psychiatry and Department of Clinical Research, Østfold Hospital, Grålum, Norway.**

Lynn Egeland Mørch-Johnsen

*

Contributions M.M., A.M., P.L. conceived the study. M.M. wrote the code and conducted the experiments. I.A., L.E.M.J. and M.M. collected and pre-processed the data cohort. M.M. and A.M. analyzed the data and results. M.M. contributed to pulling deep learning and XAI methods and conducted chart reviews. M.M. contributed to the experimental design and validation protocol. A.M. M.M. and P.L. was in charge of overall direction and planning. All authors contributed to the interpretation of the results. M.M., and A.M. visualized the study and extracted figures, and M.M. and A.M. drafted the manuscript, which was reviewed, revised and approved by all authors.

*

Corresponding author Correspondence to Michail Mamalakis or Pietro Lio

*

Ethics declarations

Competing interests

The authors declare no competing interests.

References

- [1] Ham, Y.-G., Kim, J.-H. & Luo, J.-J. Deep learning for multi-year enso forecasts. *Nature* **573**, 568–572 (2019). URL <https://doi.org/10.1038/s41586-019-1559-7>.
- [2] Reichstein, M. *et al.* Deep learning and process understanding for data-driven earth system science. *Nature* **566**, 195–204 (2019). URL <https://doi.org/10.1038/s41586-019-0912-1>.
- [3] Samek, W., Montavon, G., Lapuschkin, S., Anders, C. J. & Müller, K.-R. Explaining deep neural networks and beyond: A review of methods and applications. *Proceedings of the IEEE* **109**, 247–278 (2021).
- [4] Mamalakis, M. *et al.* Artificial intelligence framework with traditional computer vision and deep learning approaches for optimal automatic segmentation of left ventricle with scar. *Artificial Intelligence in Medicine* **143**, 102610 (2023). URL <https://www.sciencedirect.com/science/article/pii/S0933365723001240>.
- [5] Mamalakis, M. *et al.* A 3d explainability framework to uncover learning patterns and crucial sub-regions in variable sulci recognition (2023). [2309.00903](https://arxiv.org/abs/2309.00903).
- [6] Viñas, R. *et al.* Hypergraph factorization for multi-tissue gene expression imputation. *Nature Machine Intelligence* **5**, 739–753 (2023). URL <https://doi.org/10.1038/s42256-023-00684-8>.
- [7] Mamalakis, M., Macfarlane, S. C., Notley, S. V., Gad, A. K. B. & Panoutsos, G. A novel framework employing deep multi-attention channels network for the autonomous detection of metastasizing cells through fluorescence microscopy (2023). [2309.00911](https://arxiv.org/abs/2309.00911).
- [8] van der Velden, B. H. M. Explainable ai: current status and future potential. *European Radiology* (2023). URL <https://doi.org/10.1007/s00330-023-10121-4>.
- [9] Longo, L. *et al.* Explainable artificial intelligence (xai) 2.0: A manifesto of open challenges and interdisciplinary research directions. *Information Fusion*

106, 102301 (2024). URL <https://www.sciencedirect.com/science/article/pii/S1566253524000794>.

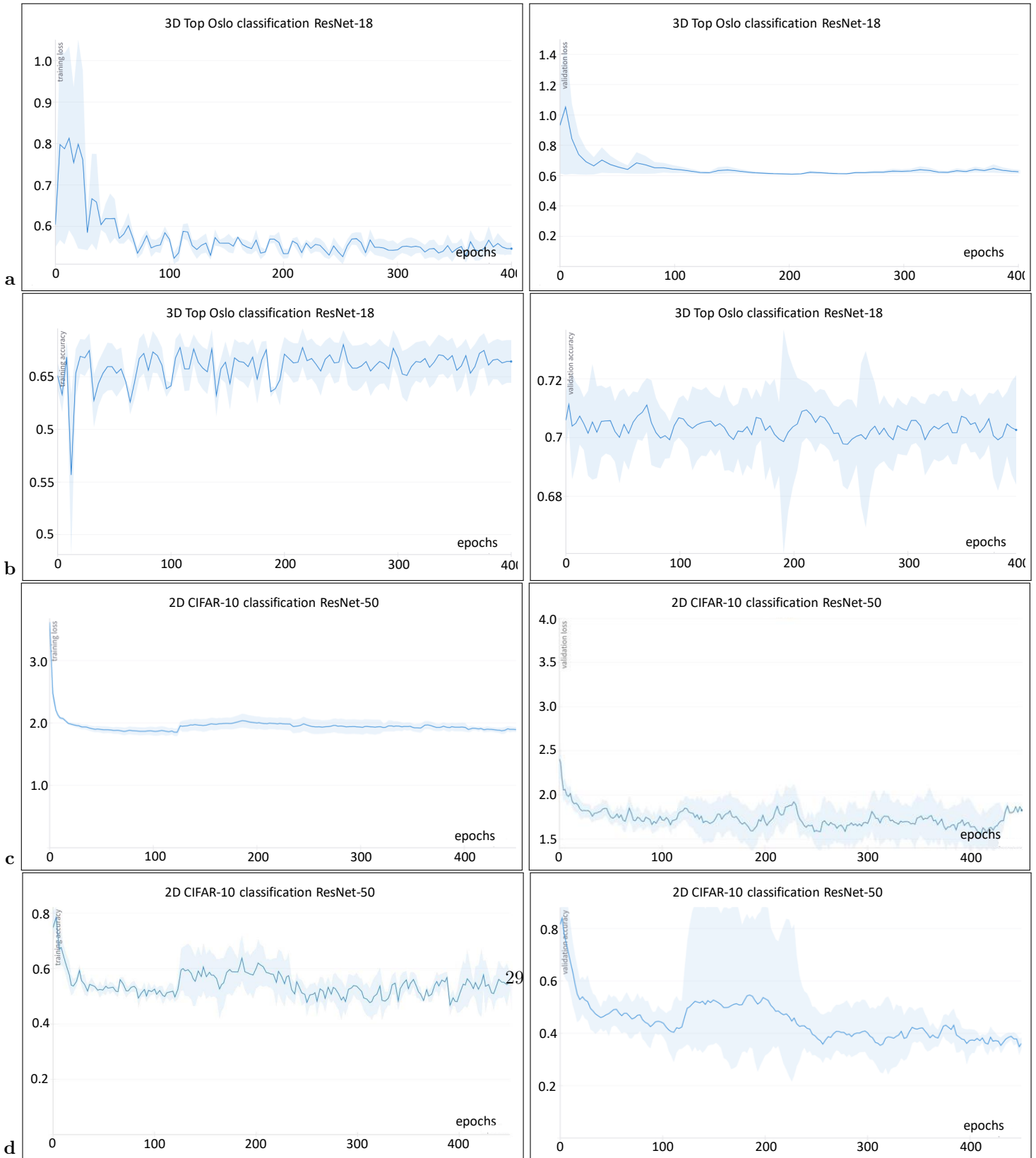
- [10] Bach, S. *et al.* On pixel-wise explanations for non-linear classifier decisions by layer-wise relevance propagation. *PLOS ONE* **10**, 1–46 (2015).
- [11] Ribeiro, M. T., Singh, S. & Guestrin, C. "why should i trust you?": Explaining the predictions of any classifier (2016). [1602.04938](https://arxiv.org/abs/1602.04938).
- [12] Rajani, N. F., McCann, B., Xiong, C. & Socher, R. Explain yourself! leveraging language models for commonsense reasoning (2019). [1906.02361](https://arxiv.org/abs/1906.02361).
- [13] Tjoa, E. & Guan, C. A survey on explainable artificial intelligence (xai): Toward medical xai. *IEEE Transactions on Neural Networks and Learning Systems* 1–21 (2020).
- [14] Mamalakis, A., Barnes, E. A. & Ebert-Uphoff, I. Investigating the fidelity of explainable artificial intelligence methods for applications of convolutional neural networks in geoscience. *Artificial Intelligence for the Earth Systems* **1**, e220012 (2022). URL <https://journals.ametsoc.org/view/journals/aies/1/4/AIES-D-22-0012.1.xml>.
- [15] Singh, A., Sengupta, S. & Lakshminarayanan, V. Explainable deep learning models in medical image analysis (2020). [2005.13799](https://arxiv.org/abs/2005.13799).
- [16] Mamalakis, A., Ebert-Uphoff, I. & Barnes, E. A. *Explainable Artificial Intelligence in Meteorology and Climate Science: Model Fine-Tuning, Calibrating Trust and Learning New Science*, 315–339 (Springer International Publishing, Cham, 2022). URL https://doi.org/10.1007/978-3-031-04083-2_16.
- [17] Mamalakis, A., Ebert-Uphoff, I. & Barnes, E. A. Neural network attribution methods for problems in geoscience: A novel synthetic benchmark dataset. *Environmental Data Science* **1**, e8 (2022).
- [18] Bach, S. *et al.* On pixel-wise explanations for non-linear classifier decisions by layer-wise relevance propagation. *PLOS ONE* **10**, 1–46 (2015). URL <https://doi.org/10.1371/journal.pone.0130140>.
- [19] Kohlbrenner, M. *et al.* Towards best practice in explaining neural network decisions with lrp (2020). [1910.09840](https://arxiv.org/abs/1910.09840).
- [20] Lundberg, S. M. & Lee, S. A unified approach to interpreting model predictions. *CoRR* **abs/1705.07874** (2017). URL <http://arxiv.org/abs/1705.07874>.
- [21] Mitchell, R., Cooper, J., Frank, E. & Holmes, G. Sampling permutations for shapley value estimation (2022). [2104.12199](https://arxiv.org/abs/2104.12199).

- [22] Jethani, N., Sudarshan, M., Covert, I., Lee, S.-I. & Ranganath, R. Fastshap: Real-time shapley value estimation (2022). [2107.07436](#).
- [23] Kolpaczki, P., Bengs, V., Muschalik, M. & Hüllermeier, E. Approximating the shapley value without marginal contributions (2024). [2302.00736](#).
- [24] Hedström, A. *et al.* Quantus: An explainable ai toolkit for responsible evaluation of neural network explanations and beyond. *Journal of Machine Learning Research* **24**, 1–11 (2023). URL <http://jmlr.org/papers/v24/22-0142.html>.
- [25] Mørch-Johnsen, L. *et al.* Auditory cortex characteristics in schizophrenia: Associations with auditory hallucinations **43**, 75–83. URL <https://academic.oup.com/schizophreniabulletin/article/43/1/75/2503785>.
- [26] Fornito, A. *et al.* Morphology of the paracingulate sulcus and executive cognition in schizophrenia **88**, 192–197. URL <https://linkinghub.elsevier.com/retrieve/pii/S0920996406003021>.
- [27] Garrison, J. R. *et al.* Paracingulate sulcus morphology is associated with hallucinations in the human brain **6**, 8956. URL <http://www.nature.com/articles/ncomms9956>.
- [28] Krizhevsky, A. *Learning multiple layers of features from tiny images* (2009). URL <https://api.semanticscholar.org/CorpusID:18268744>.
- [29] Simon, H. A. A Behavioral Model of Rational Choice. *The Quarterly Journal of Economics* **69**, 99–118 (1955). URL <https://doi.org/10.2307/1884852>.
- [30] Simon, H. A. Invariants of human behavior. *Annual Review of Psychology* **41**, 1–20 (1990). URL <https://www.annualreviews.org/content/journals/10.1146/annurev.ps.41.020190.000245>.
- [31] Simon, H. A. Rational choice and the structure of the environment. *Psychological Review* **63**, 129–138 (1956).
- [32] Mamalakis, M. *et al.* An explainable three dimension framework to uncover learning patterns: A unified look in variable sulci recognition (2024). [2309.00903](#).
- [33] Mitchell, S. C. *et al.* Paracingulate sulcus measurement protocol v2 (2023). URL <https://www.repository.cam.ac.uk/handle/1810/358381>.
- [34] Yeh, C.-K., Hsieh, C.-Y., Suggala, A. S., Inouye, D. I. & Ravikumar, P. On the (in)fidelity and sensitivity for explanations (2019). URL <https://arxiv.org/abs/1901.09392>.
- [35] Bhatt, U., Weller, A. & Moura, J. M. F. Evaluating and aggregating feature-based model explanations (2020). URL <https://arxiv.org/abs/2005.00631>.

- [36] Wang, Z., Bovik, A., Sheikh, H. & Simoncelli, E. Image quality assessment: from error visibility to structural similarity. *IEEE Transactions on Image Processing* **13**, 600–612 (2004).
- [37] He, K., Zhang, X., Ren, S. & Sun, J. Deep residual learning for image recognition. *CoRR* **abs/1512.03385** (2015). URL <http://arxiv.org/abs/1512.03385>.
- [38] Hatamizadeh, A. *et al.* Crimi, A. & Bakas, S. (eds) *Swin unetr: Swin transformers for semantic segmentation of brain tumors in mri images.* (eds Crimi, A. & Bakas, S.) *Brainlesion: Glioma, Multiple Sclerosis, Stroke and Traumatic Brain Injuries*, 272–284 (Springer International Publishing, Cham, 2022).
- [39] Ronneberger, O., Fischer, P. & Brox, T. U-net: Convolutional networks for biomedical image segmentation. *CoRR* **abs/1505.04597** (2015). URL <http://arxiv.org/abs/1505.04597>.
- [40] Dosovitskiy, A. *et al.* An image is worth 16x16 words: Transformers for image recognition at scale. *CoRR* **abs/2010.11929** (2020). URL <https://arxiv.org/abs/2010.11929>.
- [41] Sundararajan, M., Taly, A. & Yan, Q. Axiomatic attribution for deep networks (2017). [1703.01365](https://arxiv.org/abs/1703.01365).
- [42] Springenberg, J. T., Dosovitskiy, A., Brox, T. & Riedmiller, M. Striving for simplicity: The all convolutional net (2015). [1412.6806](https://arxiv.org/abs/1412.6806).
- [43] Selvaraju, R. R. *et al.* Grad-cam: Visual explanations from deep networks via gradient-based localization. *International Journal of Computer Vision* **128**, 336–359 (2019). URL <http://dx.doi.org/10.1007/s11263-019-01228-7>.
- [44] Kingma, D. P. & Ba, J. Adam: A method for stochastic optimization (2014). URL <https://arxiv.org/abs/1412.6980>.
- [45] Bell, A. J. & Sejnowski, T. J. The “independent components” of natural scenes are edge filters. *Vision Research* **37**, 3327–3338 (1997). URL <https://www.sciencedirect.com/science/article/pii/S0042698997001211>.

Extended DATA Figures

Extended DATA Fig. 1: Classification training results of 2D and 3D tasks



(a-d) The light blue shading in the panels highlights the min/max and the median loss (or accuracy) values obtained during training across various learning rates. **(a-b)** Results for the binary classification task in the 3D brain application. The utilized network is Resnet-18, trained and validated in the Top-Oslo cohort. **(c-d)** Results for the multi-class classification task in the 2D automobile/animals application. The utilized network is ResNet-50, trained and validated in the CIFAR-10 cohort.